Research Article | Vol. 28, No. 2 / 20 January 2020 / Optics Express 875
Optics EXPRESS

Radiative metasurface for thermal camouflage, illusion and messaging

JINLIN SONG, SHIYAO HUANG, YUPU MA, QIANG CHENG, RUN HU,* AND XIAOBING LUO

State Key Laboratory of Coal Combustion, School of Energy and Power Engineering, Huazhong University of Science and Technology, Wuhan 430074, China
*hurun@hust.edu.cn

Abstract: Thanks to the conductive thermal metamaterials, novel functionalities like thermal cloak, camouflage and illusion have been achieved, but conductive metamaterials can only control the in-plane heat conduction. The radiative thermal metamaterials can control the out-of-plane thermal emission, which are more promising and applicable but have not been studied as comprehensively as the conductive counterparts. In this paper, we theoretically investigate the surface emissivity of metal/insulator/metal (MIM, i.e., Au/Ge/Au here) microstructures, by the rigorous coupled-wave algorithm, and utilize the excitation of the magnetic polaritons to realize thermal camouflage through designing the grating width distribution by minimizing the temperature standard deviation of the overall plate. Through this strategy, the hot spot in the original temperature field is removed and a uniform temperature field is observed in the infrared camera instead, demonstrating the thermal camouflage functionality. Furthermore, thermal illusion and thermal messaging functionalities are also demonstrated by resorting to using such an emissivity-structured radiative metasurface. The present MIM-based radiative metasurface may open avenues for developing novel thermal functionalities via thermal metasurface and metamaterials.

1. Introduction

Artificial thermal metamaterials, albeit inheriting with blemishes like inhomogeneity and singularity, has fueled the discovery and invention of unprecedented novel phenomena, mechanisms and functionalities, like thermal cloaking, concentrating, reflecting, refracting, reversing, camouflaging, illusion, etc [1–10]. Most devices tune the in-plane heat conduction along predesigned plate with particular thermal conductivity tensors based on the transformation thermotics or scattering cancellation techniques [11–14]. However, two long-standing challenges remain formidable. One is the stringent inherent requirement of inhomogeneous parameters for the perfect tunability of heat conduction, and the other is loss of efficacy when the targets are detected from the out-of-plane direction. Trying to fix this, a general illusion thermotics strategy have been proposed to realize conductive camouflage in hemispherical space by maintaining perfect external camouflage and creating internal split illusions. However, for practical purpose, a radiative scheme, rather than a conductive one needs more attention [15–26].

In the radiative scheme, when observed by an infrared (IR) camera, an upwardly projected cross section of a target can be detected based on the preset emissivity and its real temperature. According to the working principle of an IR camera, the observed temperature is based on the detected radiation from the target surface, which include three parts, i.e., target radiation, environment reflection radiation, and air radiation. The detected temperature-dependent radiation luminance L_λ is [27]

$$L_\lambda = \varepsilon_\lambda L_{b\lambda}(T_o) + \rho_\lambda L_{b\lambda}(T_a) = \varepsilon_\lambda L_{b\lambda}(T_o) + (1 - \alpha_\lambda) L_{b\lambda}(T_a), \quad (1)$$

#378424 https://doi.org/10.1364/OE.378424
Journal © 2020 Received 7 Nov 2019; revised 11 Dec 2019; accepted 25 Dec 2019; published 6 Jan 2020

Optics EXPRESS

where T_o and T_a are the target temperature and air temperature, and ε_λ, ρ_λ, and α_λ are the surface emissivity, reflectance and absorptivity, and $L_{b\lambda}$ is the radiation luminance of blackbody. The first term on the right hand is the surface spectral radiation luminance, and the second term is the reflected environment spectral radiation luminance. The detected surface illuminance is [27]

$$E_\lambda = A_0 d^{-2}[\tau_{a\lambda} L_\lambda + \varepsilon_{a\lambda} L_{b\lambda}(T_a)], \tag{2}$$

where A_0 is the minimum viewing area of the target, d is the distance between the IR camera and the target, $\tau_{a\lambda}$ and $\varepsilon_{a\lambda}$ are the air spectral transmittance and emissivity. The radiation power is $P_\lambda = A_R E_\lambda$ and the corresponding signal voltage is $V_s = A_R \int_{\Delta\lambda} E_\lambda \phi_\lambda d\lambda$ where A_R is the lens area of the IR camera and ϕ_λ is the spectral response function (SRF). The observed temperature is then interpreted into cloud or contour figure based on the signal voltage (integrated radiation power) in certain working wavelength range, such as 2~5 μm or 8~13 μm. Outside these two IR windows, the IR radiation is strongly attenuated due to the absorption and scattering effect by the CO_2 and H_2O vapor in the air [28].

Understanding such working principle of an IR camera, we can find that, to generate equivalent pseudo detected temperature for thermal camouflage, one way is to maintain the temperature close to the ambient, and the other way is to change the surface emissivity. Comparably, since the surface temperature is not easy to maintain, the latter one attracts more attentions recently, and several radiative camouflage devices have been achieved [29–31]. Most of them are achieved by tuning the surface emissivity, absorptivity, and reflectivity based on specific phase-change materials, surface nanostructures, external optical, mechanical or electrical stimuli [32–36]. Actually, surface metal/insulator/metal (MIM) grating microstructures, including 1D/2D binary gratings and photonic crystals, have been comprehensively studied to tune the surface emissivity by employing the mechanism of surface plasmon/phonon polaritons (SPPs) or magnetic polaritons (MPs) for increasing applications like thermophotovoltaic (TPV) system, near-field microscopy and spectroscopy, and polarization manipulation [37–49]. Compared to the conductive counterparts, the dimensions of the MIM structures are usually in the μm scale, thus the temperature modulation based on MIM can be more flexible with high resolution.

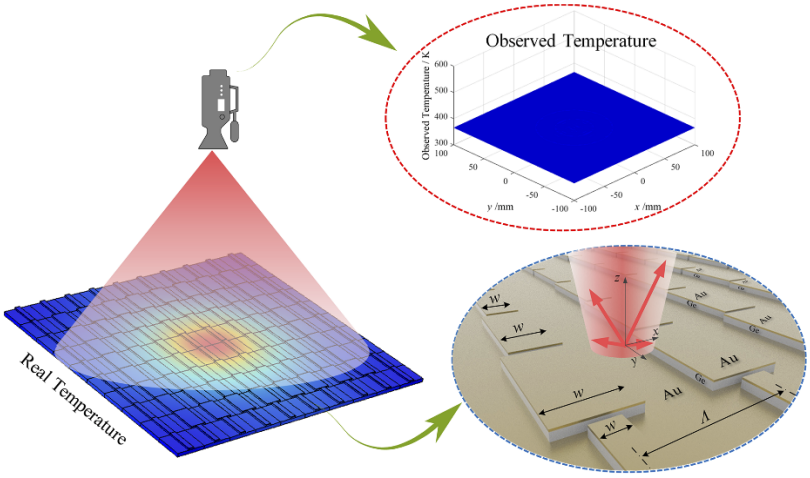

Fig. 1. Schematic for the radiative metasurface for thermal camouflage. A heat source on a plate is observed in an IR camera by interpreting the surface radiation energy into temperature field. With MIM structure engineering, a uniform temperature field is observed and the real heat source is thermally camouflaged.

Optics EXPRESS

Is it possible to extend the radiative MIM structures to achieve the out-of-plane counterpart functionalities of the conductive thermal metamaterials? If feasible, we can tune the surface radiation pixel by pixel or point by point. As shown in Fig. 1, when a heat source is located on a plate with non-uniform temperature distribution, we may still observe a uniform temperature field from an IR camera as long as the plate surface is predesigned with proper MIM structures. To examine this feasibility is the exact motivation behind this study. Note that, because MPs are insensitive to direction by nature in stark contrast to SPPs [50], MIM structures are more suitable for thermal camouflage, illusion and messaging. In this paper, we propose a general strategy to design radiative metasurfaces with different surface emissivity by controlling the MIM grating structures via tuning MPs, so as to realize these functionalities. The rigorous coupled-wave algorithm (RCWA) method is used to calculate the surface emissivity of the surface with varying MIM grating structures. The LC circuit model is applied for further discussions on the related mechanisms.

2. Methodology

The schematic of the proposed 1D MIM microstructure in a unit cell is shown in Fig. 2(a). The grating ridge is made of gold (Au) and germanium (Ge) patches with their thicknesses of $d_1 = 0.05$ μm and $d_2 = 0.2$ μm. The periodic arrays of patches are deposited on an opaque gold substrate with the thickness of d_3=0.5 μm, so that the transmittance can be neglected. The period Λ is fixed as 3.8 μm, and the grating width w is tuned to control the surface radiation for desired emissivity. Such MIM microstructures can be fabricated with nanoimprint, interference lithography, and electron-beam lithography techniques [42]. The RCWA program is used to calculate the wavelength-dependent reflectance R_λ and transmittance T_λ with considering a total of 101 diffraction orders. According to Kirchhoff's law, the wavelength-dependent surface emissivity is obtained as $\varepsilon_\lambda = 1-R_\lambda-T_\lambda$. For 1D MIM structures in this work, all diffracted waves lie in the x-z plane, so that MPs can be only excited for transverse magnetic (TM) waves. Consequently, only the thermal emission for TM waves is considered here. Note that, such a strategy can be easily generalized to a more universal application by constructing a 2D metasurface which supports MPs for both TM and TE waves [51].

The emissivity spectra with varied grating widths are shown in Fig. 2(b). With the increase of grating width from 0.9 μm to 1.4 μm, the emissivity peak is red-shifted from ~7 μm to ~14.8 μm, while the emissivity intensity increases from 0.78 to 0.98. Furthermore, we find the lower and upper bounds for the grating widths are 0.7 and 1.65 μm, whose emissivity spectrum peaks are less than 8 μm or much higher than 13 μm and the infrared radiation power integrations in this range can be neglected. These peaks originate from MPs supported by the MIM structure, which refer to the strong coupling of the magnetic resonance in the MIM structures with the external EM fields [51]. The MPs resonance wavelength can be predicted by the inductor-capacitor (LC) circuit theory, and Fig. 2(c) gives the equivalent LC circuit for the MIM structure, in which the arrows point out the direction of electric currents. In the LC circuit model, $L_\mathrm{m} = 0.5\mu_0 w d_2/l$, denotes the parallel-plate inductance separated by the intermediate Ge layer, where μ_0 is the permeability of vacuum and l is the patch length in the y direction. $C_\mathrm{g} = \varepsilon_0 d_1 l/(\Lambda - w)$ is the capacitance of the gap between the neighboring grating ridges, where ε_0 is the permittivity of vacuum. $C_\mathrm{m} = c_1\varepsilon_\mathrm{Ge}\varepsilon_0 wl/d_2$ refers to the parallel-plate capacitance between two layers induced by the Ge layer, where c_1=0.19 is a numerical factor which considers non-uniform charge distribution, and $\varepsilon_\mathrm{Ge} = 16$ is the dielectric function of Ge [52]. Because the drifting electrons also contribute moderately to the total inductance in this MIM structure, and the kinetic inductance is expressed as $L_e = -w/(\omega^2 d_\mathrm{eff} l\varepsilon_0\varepsilon'_\mathrm{Au})$, where ω is the angular frequency, ε'_Au is the real part of dielectric function of Au which can be obtained from the Drude model where the detailed parameters are taken from Ref. [53], and d_eff is the effective thickness for electric currents in the Au patch layer as $d_\mathrm{eff} = \delta$ for $\delta < d_2$, and $d_\mathrm{eff} = d_2$ otherwise, where the power

Optics EXPRESS

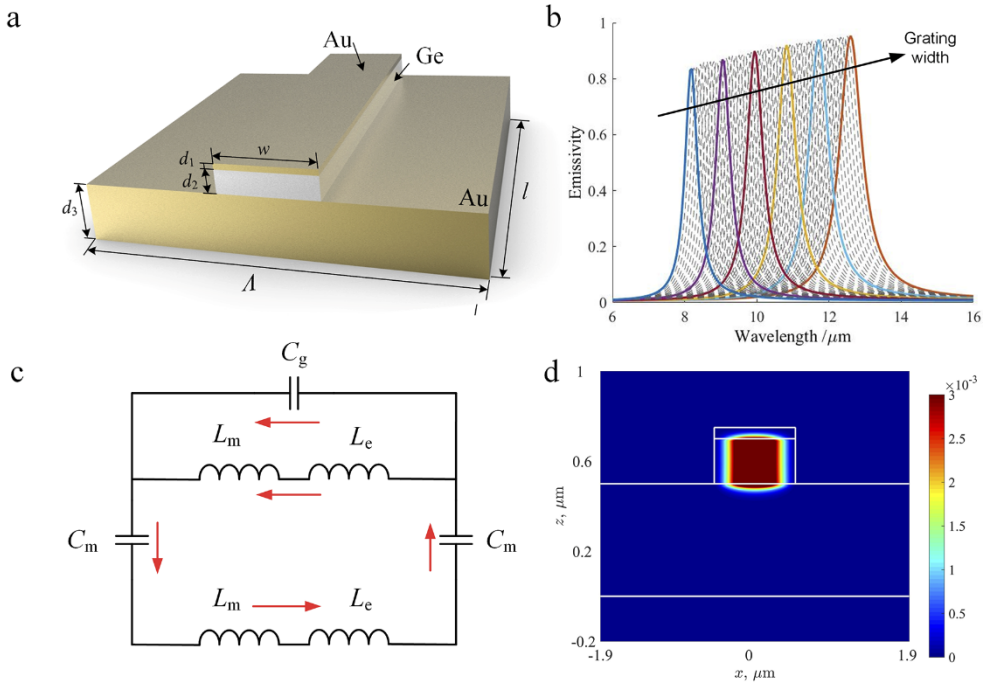

Fig. 2. (a) Schematic for the single Au/Ge/Au MIM structure, in which a thin-layer Ge spaces Au grating and Au substrate. The MIM structure is deposited at the center of the period Λ. The grating width w is screened from 0.9 μm to 1.4 μm and the corresponding surface emissivity spectra are plotted in (b) where the wavelength range is 6~16 μm. (c) Equivalent LC circuit model for the fundamental MP mode of the single MIM structure. (d) EM field distribution at the MP resonance wavelength of 8.39 μm.

penetration depth $\delta = \lambda/4\pi\kappa$ with λ the incident wavelength and κ the extinction coefficient of Au. Then, the impedance of a single MIM structure can be expressed as [39,43]

$$Z_{\text{single}} = \frac{i\omega(L_m + L_e)}{1 - \omega^2(L_m + L_e)C_g} + i\omega(L_m + L_e) - \frac{2i}{\omega C_m}. \tag{3}$$

Then, by zeroing Z_{single}, resonance wavelengths of $\lambda_R = 8.38$, 10.25 and 13.0 μm can be obtained for $w = 0.9$, 1.1 and 1.4 μm, respectively, which match well with the RCWA results. According to Lenz's law, due to the time-varying magnetic field in the y direction, an oscillating current can be produced which endows the MIM structure with the diamagnetism by generating a reversed magnetic field. In order to elucidate the underlying mechanism, Fig. 2(d) presents the magnetic field distribution at the MP resonance wavelength of 8.39 μm. The white lines denote the profile of the MIM structure. The contour shows the magnetic field intensity in the y direction, i.e., $|H_y|^2$. It can be observed that, the strong magnetic field is confined in Ge layer which demonstrates the excitation of MPs and corresponds to the emissivity peak in Fig. 2(b).

3. Results and discussion

Let us now focus on the integrated radiation power (calculated by thermal emission for TM waves) in the working wavelength range 8~13 μm which is directly related to the observed temperature in the IR camera and differs greatly due to the frequency shift of the emissivity peak. Initially, a certain real temperature distribution is pre-generated, as shown in Figs. 3(a)

Optics EXPRESS

and 4(a). The temperature curve in Fig. 3(a) is the center line of Fig. 4(a). The dimension of the Si plate is 200 mm × 200 mm × 5 mm, and the size of the central 15 Watt heat source is 5 mm × 5 mm. All the surfaces are immersed in the air with natural air convective coefficient of 2 W/(m^2·K) at room temperature of 20 °C. As a result, the maximum temperature along the center line is 392.1 K and the boundary is at 381.7 K. To camouflage the heat source via emissivity engineering, we divide the surface into M × N unit cells (101 × 101, here), and we deposit different MIM structures on each unit cell. For an emitter with a finite length along the axis of strips where the Stefan-Boltzmann's law does not apply [54], the absorption cross section, which is calculated through considering the total scattering fields, is required to characterize its emission property. These considerations have limited effects on the performance evaluation, but vastly increase the difficulty of predesign. In this work, the emitter has a period of 3.8 μm which is far less (~50 times) than the strip length of a unit cell. This makes it reasonable to regard the unit cell as a 1D structure. Due to the invariance of the environment, geometry configuration and experimental setup, the air temperature and spectral transmittance/absorptivity, viewing cross-sectional area, distance, solid angle and lens area, thus we only consider the integrated surface radiation power and neglect the dependence of SRF for simplification hereinafter, which is enough for the proof-of-concept demonstration. According to the Planck's law, the integrated radiation power is calculated as [55]

$$P = \int_{\lambda_1}^{\lambda_2} \varepsilon_\lambda E_{b\lambda} d\lambda = \int_{\lambda_1}^{\lambda_2} \varepsilon_\lambda \frac{C_1 \lambda^{-5}}{e^{C_2/(\lambda T_o)} - 1} d\lambda, \tag{4}$$

where $C_1 = 3.743\times10^{-16}$ W·m^3 and $C_2 = 1.4387\times10^{-2}$ m·K are the two Planck constants. Though the local temperature of each unit cell is different, we tune the spectral emissivity of each cell to make their integrated radiation power at the same/approximate level. Therefore, a same observed temperature distribution can be detected in the IR camera. We screen the grating width of each unit cell to maintain the standard deviation (STD) σ of all the integrated radiation power as minimum as possible by $\sigma = \sqrt{\sum_{k=1}^{k=M\times N} (P_k - \bar{P})} \Big/ (M \times N)$. Figure 3(b) shows the integrated radiation power variation of five typical unit cells along the center line of the plate with different grating widths. It is seen that higher temperature corresponds to higher radiation power in general. To quantify one desired radiation power P_d that all the unit cells can achieve with selected grating width (emissivity), we decrease the P_d gradually and calculate the corresponding STD until the STD is the minimum. Using this method, P_d is quantified as $P_d = 72.403$ W/m^3, and the widths of these unit cell are selected one by one denoted by the vertical dash lines in Fig. 3(b). The observed temperature curve is shown in Fig. 3(c) according to the Stefan-Boltzmann law and the preset constant surface emissivity of the IR camera is the average value of the all the unit cells. Compared with Fig. 3(a), it is seen that the observed temperature is much uniform and the STD is only 0.144. The grating width distribution of all the unit cells is shown in Fig. 3(d), and it is seen that the width in the center is the smallest, and the width fluctuates from the center to the boundary. The distribution of the selected emissivity for all the unit cells and the observed temperature for the whole plate is seen in Figs. 4(b) and 4(e). It is seen that the observed temperature is uniform and the real heat source is camouflaged in the background, demonstrating the thermal camouflage function by such emissivity engineering.

Based on the observed uniform temperature, we can further engineer the local surface emissivity to realize thermal illusions and thermal messaging. We randomly select four rectangular subareas to possess much larger local emissivity than the remaining surface. For this end, we take advantage of the LC circuit theory to reversely predesign the patch width of the MIM structure for a certain resonance wavelength, and combine them to compose a multi-band MIM structure (perfect emitter hereinafter), as shown in Fig. 5(a). Such perfect emitter structure is composed by multiple MIM gratings with 8 widths (w_1=0.9, w_2=0.95, w_3=1, w_4=1.05 w_5=1.1, w_6=1.2,

Optics EXPRESS

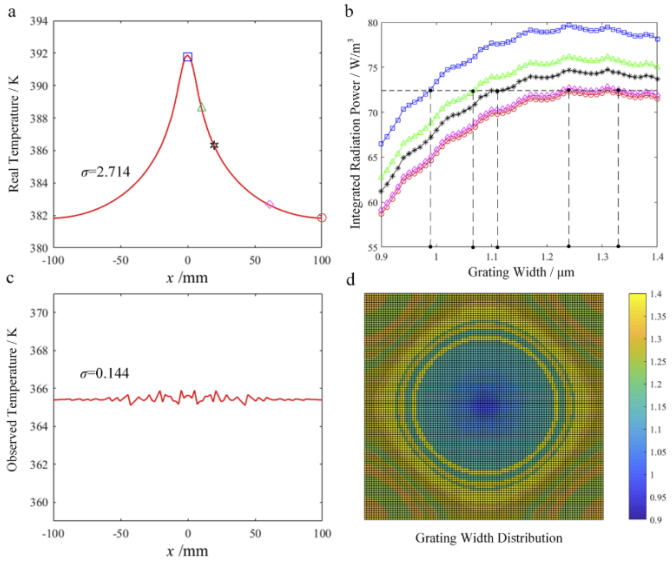

Fig. 3. (a) Temperature distribution along the center line of the simulated plate with the heat source located at the center. The standard deviation (STD) is $\sigma = 2.714$. (b) Integrated radiation power with varied grating width of five typical points in (a). A proper radiation power is selected by minimizing the STD of the integrated radiation power of all points on the simulated plate. The corresponding grating widths of the typical five points can be quantified as the vertical dash lines denote. (c) Observed pseudo temperature converted from the integrated radiation power in the infrared camera. The observed temperature is much uniform with a small STD $\sigma = 0.144$. (d) Grating width distribution of all the points on the simulated plate with the same quantifying method in (b).

w_7=1.3, and w_8=1.4 μm) of 1D single MIM structure and the layer thickness is maintained the same as previous single MIM structure. The spectral emittance of the perfect emitter is given in Fig. 5(b). Clearly, the emittance spectrum shows a plateau with the value of around 0.9 in the 8∼13 μm range even under different incident angles. Such angular insensitivity enables the similar detected temperature when the IR camera is rotated with respect to the normal direction. To explain the broad-band high emittance, Figs. 5(c)–5(e) give the magnetic field distribution at the MP resonance wavelengths of 8.25, 10.12 and 12.73 μm, respectively. In Fig. 5(c), it can be seen that, at 8.25 μm, the left top MIM of the perfect emitter shows a strong confined magnetic field in Ge layer, indicating that the emittance peak at 8.25 μm is attributed to the MPs of left top MIM unit. Also, the emittance peak at 12.73 μm is attributed to the MPs of right bottom MIM unit, of which the magnetic field distribution is shown in Fig. 5(e). While in Fig. 5(d), it can be seen that, there exist high confined magnetic fields in two MIM units simultaneously, which mean that the high emittance at 10.12 μm is due to the MPs of two MIM structures. In a word, the high multi-band emittance of the perfect emitter is attributed to the hybridization of separated MPs in the multiple MIM units. We also can understand this by the equivalent LC circuit for the multiple MIM structure. For a multiple MIM structure consisting of several MIM subunits, the enhanced electromagnetic field in one subunit is strongly confined without coupling to other subunits when MPs are excited, so that each MIM subunit behaves as an isolated unit [56]. Therefore, the total impedance of the multiple MIM structure can be expressed using the parallel LC model as $\frac{1}{Z_{\text{multiple}}} = \sum_{j}^{N} \frac{1}{Z_{\text{single},j}}$, where $Z_{\text{single},j}$ (obtained by Z_{single} in Eq. (3)) is the impedance of the j-th subunit ($j = 1, 2, \ldots, N$, where N is the total number of subunits) to predict the multiple

Optics EXPRESS

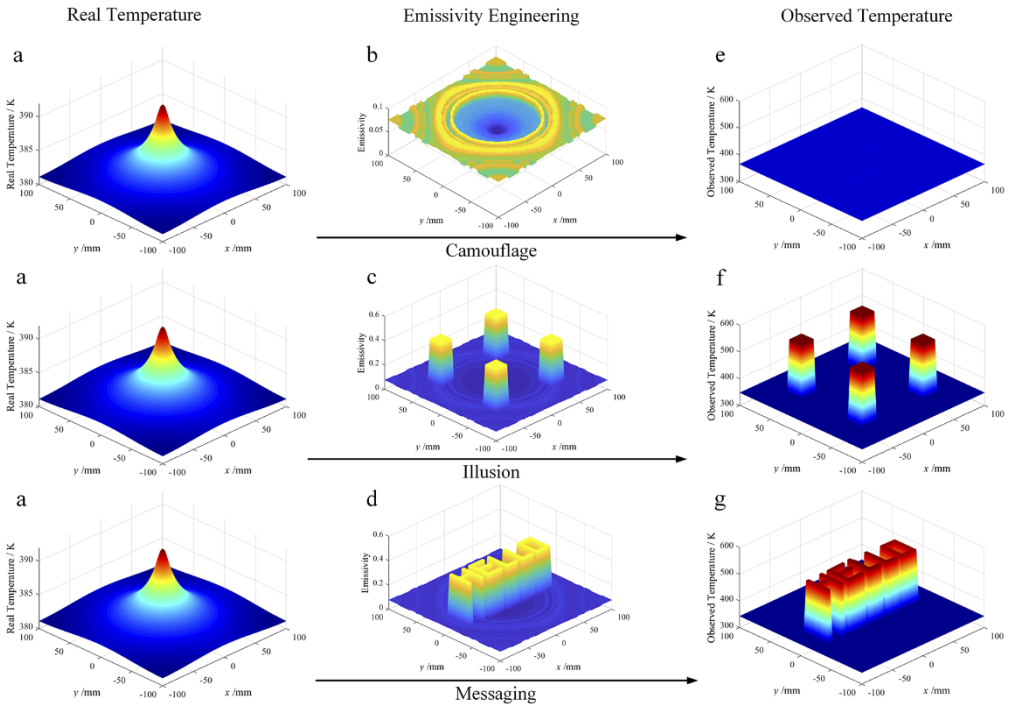

Fig. 4. Demonstration of thermal camouflage, illusion and messaging functionalities. (a) Original temperature field of a plate with a heat source in the center. An obvious hot spot exists in the temperature field. (b-d) Surface emissivity distribution for different applications. (e) The hot spot is camouflaged and a uniform temperature is observed instead, demonstrating the thermal camouflage functionality. (f) Four separated hot spots emerge on the basis of the uniform temperature field in (e), demonstrating the thermal illusion functionality. (g) The heat signature of "HELLO" is observed on the basis of the uniform temperature field in (e), demonstrating the thermal messaging functionality.

resonant peaks [57]. It can be seen that, any subunit having a zero impedance, i.e., $Z_{\text{single},j} = 0$, enables the total impedance of the multiple MIM structure to be zero, i.e., $Z_{\text{multiple}} = 0$. With the perfect emitter in four separated rectangular subareas, four hot spots emerge in Fig. 4(f) from the uniform pseudo temperatures in Fig. 4(e), which implies that not only the original heat source is camouflaged, but also four illusion heat sources are generated to further confuse the observers. This is the thermal illusion functionality. Further, if we arrange the selected subarea distribution, we can further realize the thermal messaging. For instance, as shown in Fig. 4(g), the heat signature of "HELLO" emerges by properly engineering the surface emissivity and local microstructure on the plate. It is perceived that more letters, graphs, and information can be realized through the same strategy.

The primary idea in this paper is to engineer the surface emissivity distribution to realize thermal camouflage, illusion and messaging functionalities. Although these functionalities have been realized in static conductive thermal metamaterials, they have not been achieved in the dynamic radiative thermal metasurfaces based on the MIM structures. The performance of the present functionalities can be further improved if we can construct a larger database of the optional surface emissivity with varied MIM widths. Thus, the integrated power according to Eq. (4) can be varied larger, which enables to camouflage the hot spot with a larger temperature difference in respect to the whole temperature field. One may ask how much difference thermal

Optics EXPRESS

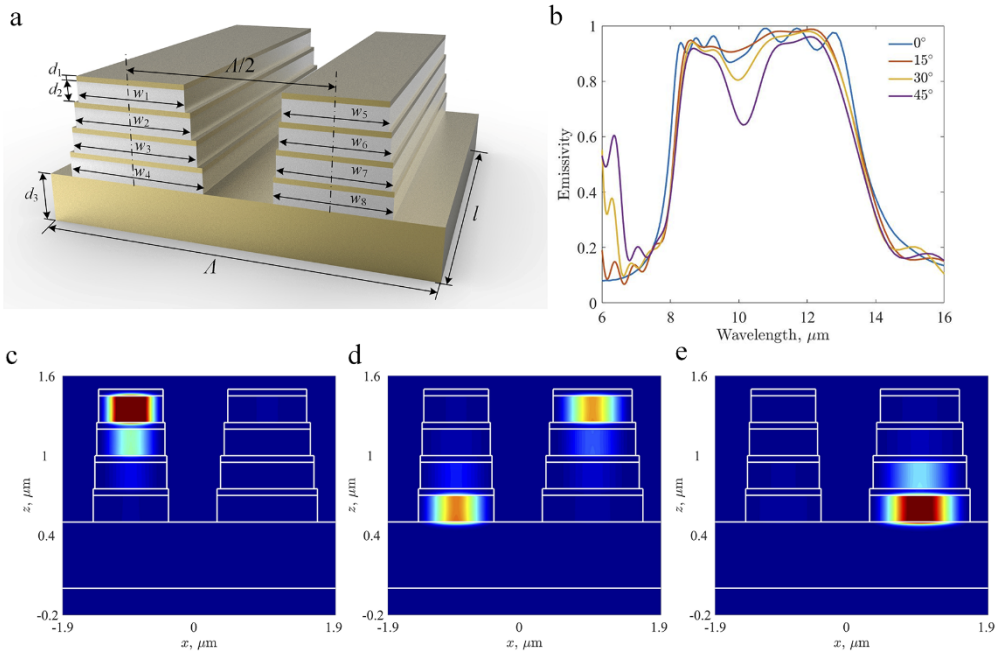

Fig. 5. (a) Schematic for the multiple MIM structure with 8 different widths (perfect emitter hereinafter). The period and the thickness of each layer are maintained the same. (b) Emission spectrum for the perfect emitter at different incident angles. (c)-(e) EM field distribution of the perfect emitter at the MP resonance wavelength of 8.25, 10.12 and 12.73 μm, respectively.

convection and radiation will make to the original temperature field. Taking the center unit in Fig. 4(e) as an example, the heat flux transferred by thermal conduction, convection, and radiation are 0.44 W, 7.9×10^{-4} W, and 1.87×10^{-4} W, respectively. It is because that the temperature difference between the plate and the ambient air is not that large, so that the proposed thermal camouflage performance will be maintained even with consideration of thermal convection and radiation. Moreover, the current study is demonstrated by the 1D MIM structure, and we can generalize this strategy through 2D MIM metasurfaces to achieve more universe functionalities. It is expected that the proposed 1D MIM structures and the validated strategy can provide hints and inspirations for further optimization and practical application. We can also extend to MIM structures of other materials, say refractory materials like tungsten, for very high temperature applications [39].

4. Conclusions

In summary, we demonstrate the feasibility of radiative metasurfaces to realize thermal camouflage, illusion and messaging by structuring the surface emissivity through MIM microstructures. The surface emissivity of the Au/Ge/Au gratings are calculated by the RCWA algorithm with varied grating width, which generate the MIM database for surface microstructure optimization. The proper grating width distribution is quantified by minimizing the temperature standard deviation (STD) on the whole plate. Using this strategy, the hot spot in the original temperature field is removed and the observed temperature field is much uniform, which can realize more satisfying thermal camouflage effect, compared with the conductive thermal metamaterials. Further, a perfect emitter is designed by stacking multiple MIM structures, whose emissivity is much larger

Optics EXPRESS

and broader in the 8~13 μm and insensitive to the incident angles. The underlying mechanism for the broad emission spectrum is ascribed to the excitation of the multiple MPs which can be demonstrated by the equivalent LC theory. By properly arranging the distribution of the perfect emitter, thermal illusion and thermal messaging functionalities are also demonstrated. The present may open avenues for developing novel thermal applications via thermal metasurface and metamaterials.

Funding

National Natural Science Foundation of China (51606074, 51625601, 51676077, 51806070); Ministry of Science and Technology of the People's Republic of China (2017YFE0100600); China Postdoctoral Science Foundation (2018M632849).

Disclosures

The authors declare no conflicts of interest.

References

1. S. Narayana and Y. Sato, "Heat flux manipulation with engineered thermal materials," Phys. Rev. Lett. **108**(21), 214303 (2012).
2. T. C. Han, X. Bai, J. T. L. Thong, B. W. Li, and C. W. Qiu, "Full control and manipulation of heat signatures: Cloaking, Camouflage and thermal metamaterial," Adv. Mater. **26**(11), 1731–1734 (2014).
3. R. Schittny, M. Kadic, S. Guenneau, and M. Wegener, "Experiments on transformation thermodynamics: Molding the flow of heat," Phys. Rev. Lett. **110**(19), 195901 (2013).
4. R. Hu, S. Huang, M. Wang, X. B. Luo, J. Shiomi, and C. W. Qiu, "Encrypted thermal printing with regionalization transformation," Adv. Mater. **31**(25), 1807849 (2019).
5. C. Z. Fan, Y. Gao, and J. P. Huang, "Shaped graded materials with an apparent negative thermal conductivity," Appl. Phys. Lett. **92**(25), 251907 (2008).
6. R. Hu, B. Xie, J. Y. Hu, Q. Chen, and X. B. Luo, "Carpet thermal cloak realization based on the refraction law of heat flux," EPL **111**(5), 54003 (2015).
7. R. Hu, X. L. Wei, J. Y. Hu, and X. B. Luo, "Local heating realization by reverse thermal cloak," Sci. Rep. **4**(1), 3600 (2015).
8. S. Guenneau, C. Amra, and D. Veynante, "Transformation thermodynamics: cloaking and concentrating heat flux," Opt. Express **20**(7), 8207–8218 (2012).
9. R. Hu and X. B. Luo, Two-dimensional phonon engineering triggers microscale thermal functionalities, Natl. Sci. Rev. nwz114, https://doi.org/10.1093/nsr/nwz114.
10. R. Hu, S. Zhou, X. Yu, and X. B. Luo, "Exploring the proper experimental conditions in 2D thermal cloaking demonstration," J. Phys. D: Appl. Phys. **49**(41), 415302 (2016).
11. N. I. Zhuludev and Y. S. Kivshar, "From metamaterials to metadevices," Nat. Mater. **11**(11), 917–924 (2012).
12. H. Y. Chen, C. T. Chan, and P. Sheng, "Transformation optics and metamaterials," Nat. Mater. **9**(5), 387–396 (2010).
13. T. C. Han, X. Bai, D. L. Gao, J. T. L. Thong, B. W. Li, and C. W. Qiu, "Experimental demonstration of a bilayer thermal cloak," Phys. Rev. Lett. **112**(5), 054302 (2014).
14. H. Xu, X. Shi, F. Gao, H. Sun, and B. Zhang, "Ultrathin three-dimensional thermal cloak," Phys. Rev. Lett. **112**(5), 054301 (2014).
15. J. B. Pendry, D. Schurig, and D. R. Smith, "Controlling electromagnetic fields," Science **312**(5781), 1780–1782 (2006).
16. U. Leonhardt, "Optic conformal mapping," Science **312**(5781), 1777–1780 (2006).
17. D. Schurig, J. J. Mock, B. J. Justice, S. A. Cummer, J. B. Pendry, A. F. Starr, and D. R. Smith, "Metamaterial electromagnetic cloak at microwave frequencies," Science **314**(5801), 977–980 (2006).
18. H. Y. Chen and C. T. Chan, "Acoustic cloaking and transformation acoustics," J. Phys. D: Appl. Phys. **43**(11), 113001 (2010).
19. M. Liu, Z. L. Mei, X. Ma, and T. J. Cui, "DC illusion and its experimental verification," Appl. Phys. Lett. **101**(5), 051905 (2012).
20. F. Magnus, B. Wood, J. Moore, K. Morrison, G. Perkins, J. Fyson, M. C. K. Wiltshire, D. Caplin, L. F. Cohen, and J. B. Pendry, "A dc magnetic metamaterial," Nat. Mater. **7**(4), 295–297 (2008).
21. R. Mach-Batlle, A. Parra, S. Laut, N. D. Valle, C. Navau, and A. Sanchez, "Magnetic illusion: transforming a magnetic object into another object by negative permeability," Phys. Rev. Appl. **9**(3), 034007 (2018).
22. Y. S. Zhao, D. Liu, J. Chen, L. Y. Zhu, A. Belianinov, O. S. Ovchinnikowa, R. R. Unocic, M. J. Burch, S. Kim, H. Hao, D. S. Pickard, B. W. Li, and J. T. L. Thong, "Engineering the thermal conductivity along an individual silicon nanowire by selective helium ion irradiation," Nat. Commun. **8**(1), 15919 (2017).

Optics EXPRESS

23. J. Lee, W. Lee, G. Wehmeyer, S. Dhuey, D. L. Olynick, S. Cabrini, C. Dames, J. J. Urban, and P. D. Yang, "Investigation of phonon coherence and backscattering using silicon nanomeshes," Nat. Commun. **8**(1), 14054 (2017).
24. Z. Q. Ye and B. Y. Cao, "Nanoscale thermal cloaking in graphene via chemical functionalization," Phys. Chem. Chem. Phys. **18**(48), 32952–32961 (2016).
25. R. Hu, S. L. Zhou, Y. Li, D. Y. Lei, X. B. Luo, and C. W. Qiu, "Illusion thermotics," Adv. Mater. **30**(22), 1707237 (2018).
26. S. L. Zhou, R. Hu, and X. B. Luo, "Thermal illusion with twinborn-like heat signatures," Int. J. Heat Mass Transfer **127**, 607–613 (2018).
27. M. Vollmer and K. P. Möllmann, *Infrared thermal imaging: fundamentals, research and applications*, John Wiley & Sons, 2017.
28. G. A. Rao and S. P. Mahulikar, "Effect of atmospheric transmission and radiance on aircraft infrared signatures," J. Aircr. **42**(4), 1046–1054 (2005).
29. L. L. Zhou, S. Huang, M. Wang, R. Hu, and X. B. Luo, "While rotating while cloaking," Phys. Lett. A **383**(8), 759–763 (2019).
30. L. Xiao, H. Ma, J. Liu, W. Zhao, Y. Jia, Q. Zhao, K. Liu, Y. Wu, Y. Wei, S. Fan, and K. Jiang, "Fast adaptive thermal camouflage based on flexible VO^2/Graphene/CNTN thin films," Nano Lett. **15**(12), 8365–8370 (2015).
31. C. Xu, G. T. Stiubianu, and A. A. Gorodetsky, "Adaptive infrared-reflecting systems inspired by cephalopods," Science **359**(6383), 1495–1500 (2018).
32. O. Salihoglu, H. B. Uzlu, O. Yakar, S. Aas, O. Balci, N. Kakenov, S. Balci, S. Olcum, S. Suzer, and C. Kocabas, "Graphene based adaptive thermal camouflage," Nano Lett. **18**(7), 4541–4548 (2018).
33. M. J. Moghimi, G. Lin, and H. R. Jiang, "Broadband and ultrathin infrared stealth sheets," Adv. Eng. Mater. **20**(11), 1800038 (2018).
34. X. Liu and W. J. Padilla, "Reconfigurable room temperature metamaterial infrared emitter," Optica **4**(4), 430–433 (2017).
35. X. L. Liu and Z. M. Zhang, "Near-Field Thermal Radiation between Metasurfaces," ACS Photonics **2**(9), 1320–1326 (2015).
36. X. Xie, X. Li, M. Pu, X. Ma, K. Liu, Y. Guo, and X. Luo, "Plasmatic metasurfaces for simultaneous thermal infrared invisibility and holographic illusion," Adv. Funct. Mater. **28**(14), 1706673 (2018).
37. Y. X. Cui, K. H. Fung, J. Xu, H. J. Ma, Y. Jin, S. L. He, and N. X. Fang, "Ultrabroadband light absorption by a sawtooth anisotropic metamaterial slab," Nano Lett. **12**(3), 1443–1447 (2012).
38. J. J. Greffet, R. Carminati, K. Joulain, J. P. Mulet, S. Mainguy, and Y. Chen, "Coherent emission of light by thermal sources," Nature **416**(6876), 61–64 (2002).
39. N. Dahan, Y. Gorodetski, K. Frischwasser, V. Kleiner, and E. Hasman, "Geometric Doppler effect: spin-split dispersion of thermal radiation," Phys. Rev. Lett. **105**(13), 136402 (2010).
40. J. L. Song, H. Wu, Q. Cheng, and J. M. Zhao, "1D trilayer films grating with W/SiO2/W structure as a wavelength-selective emitter for thermophotovoltaic applications," J. Quant. Spectrosc. Radiat. Transfer **158**, 136–144 (2015).
41. J. L. Song, M. T. Si, Q. Cheng, and Z. X. Luo, "Two-dimensional trilayer grating with a metal/insulator/metal structure as a thermophotovoltaic emitter," Appl. Opt. **55**(6), 1284–1290 (2016).
42. L. P. Wang and Z. M. Zhang, "Resonance transmission or absorption in deep grating explained by magnetic polaritons," Appl. Phys. Lett. **95**(11), 111904 (2009).
43. Y. Shuai, H. P. Tan, and Y. C. Liang, "Polariton-enhanced emittance of metallic–dielectric multilayer structures for selective thermal emitters," J. Quant. Spectrosc. Radiat. Transfer **135**, 50–57 (2014).
44. L. P. Wang and Z. M. Zhang, "Wavelength-selective and diffuse emitter enhanced by magnetic polaritons for thermophotovoltaics," Appl. Phys. Lett. **100**(6), 063902 (2012).
45. X. L. Liu, T. Tyler, T. Starr, A. F. Starr, N. M. Jokerst, and W. J. Padilla, "Taming the blackbody with infrared metamaterials as selective thermal emitters," Phys. Rev. Lett. **107**(4), 045901 (2011).
46. C. C. Wu, N. Arju, G. Kelp, J. A. Fan, J. Dominguez, E. Gonzales, E. Tutuc, I. Brener, and G. Shvets, "Spectrally selective chiral silicon metasurfaces based on infrared Fano resonances," Nat. Commun. **5**(1), 3892 (2014).
47. B. Zhao, J. Zhao, and Z. M. Zhang, "Enhancement of near-infrared absorption in graphene with metal gratings," Appl. Phys. Lett. **105**(3), 031905 (2014).
48. J. L. Song and Q. Cheng, "Near-field radiative heat transfer between graphene and anisotropic magneto-dielectric hyperbolic metamaterials," Phys. Rev. B **94**(12), 125419 (2016).
49. J. L. Song, L. Lu, Q. Cheng, and Z. X. Luo, "Surface Plasmon-Enhanced Optical Absorption in Monolayer MoS2 with One-Dimensional Au Grating," J. Quant. Spectrosc. Radiat. Transfer **211**, 138–143 (2018).
50. H. Chalabi, A. Alù, and M. L. Brongersma, "Focused thermal emission from a nanostructured SiC surface," Phys. Rev. B **94**(9), 094307 (2016).
51. Z. M. Zhang, *Nano/microscale heat transfer*. McGraw-Hill: New York; 2007.
52. E. D. Palik, *Handbook of optical constants of solids*. Academic press, 1998.
53. P. O. Chapuis, S. Volz, C. Henkel, K. Joulain, and J. J. Greffet, "Effects of spatial dispersion in near-field radiative heat transfer between two parallel metallic surfaces," Phys. Rev. B **77**(3), 035431 (2008).
54. S. A. Biehs and P. Ben-Abdallah, "Revisiting super-Planckian thermal emission in the far-field regime," Phys. Rev. B **93**(16), 165405 (2016).

Optics EXPRESS

55. J. J. Foley, C. Ungaro, K. Sun, M. C. Gupta, and S. K. Gray, "Design of emitter structures based on resonant perfect absorption for thermophotovoltaic applications," Opt. Express **23**(24), A1373–A1387 (2015).
56. N. Engheta, "Circuits with light at nanoscales: optical nanocircuits inspired by metamaterials," Science **317**(5845), 1698–1702 (2007).
57. R. Feng, J. Qiu, L. Liu, W. Ding, and L. Chen, "Parallel LC circuit model for multi-band absorption and preliminary design of radiative cooling," Opt. Express **22**(S7), A1713–A1724 (2014).